Chemical Engineering Journal 442 (2022) 136256

Contents lists available at ScienceDirect

Chemical Engineering Journal

journal homepage: www.elsevier.com/locate/cej

Carbon Nanotube Interwoven Polyhedrons with Inside-out Lithiophilic Gradients toward Stable Lithium Metal Battery

Xinhui Chen [1], Zhaohuai Li [1], Yan Li, Chunli Shen, Cheng Zhou, Xingnian Tan, Kaijian Yan, Ge Zhang, Xu Xu *

State Key Laboratory of Advanced Technology for Materials Synthesis and Processing, International School of Materials Science and Engineering, Wuhan University of Technology, Wuhan 430070, Hubei, PR China

ARTICLE INFO

Keywords:
Carbon-based materials
Metal organic framework
Gradient design
Lithium deposition

ABSTRACT

Lithium metal is one of the most potential anode materials for secondary batteries with high energy density. Nevertheless, the uncontrolled dendrite growth, fragile solid electrolyte interphase and theoretical infinite volume expansion during repeated plating/stripping process cause low Coulombic efficiency, short cycle life, and safety hazard. Carbon nanotube interwoven polyhedrons evolved from ZIF-8@ZIF-67 core–shell framework with inside-out lithiophilic gradients are prepared for lithium metal accommodation. The well-designed architecture with decreasing gradient of the main lithiophilic content ZnO from the inside out enables dendrite-free lithium deposition and stripping, and the outer interwoven carbon nanotubes induced by Co nanoparticles provide an optimal path to guide the diffusion of Li ion reduction from inside to outside as well as excellent electron conduction network for the whole anode. As the lithium metal host, the average Coulombic efficiency of lithium metal batteries can reach up to 98.2% (200 cycles) at 1 mA cm^{-2}, and an extended lifespan (1500 h) is achieved at 3 mA cm^{-2}. As was expected, outstanding capacity retention (82.7% after 300 cycles) with a competitive high-mass-loading (18.3 mg cm^{-2}) $LiFePO_4$ cathode at 1 C is realized. This structure design concept expands a promising application pathway of abundant carbon-based materials in lithium metal batteries.

1. Introduction

The strong demand for electric vehicles and large-scale energy storage has promoted the rapid expansion of secondary batteries with high energy density and safe full life [1-6]. Lithium (Li) metal is considered as the ultimate anode material for lithium metal batteries (LMBs) giving the credit to its super-high theoretical specific capacity (3860 mAh g^{-1}) and dominant redox potential (-3.04 V vs. standard hydrogen electrode) [7], which raises the practical energy–density ceiling for the next generation of LMBs, including Li-sulfur battery, Li-oxygen battery, and Li-intercalation type cathode batteries [8-10]. Despite the promising application prospect of Li metal anode, it still faces several fatal challenges, including the uncontrolled dendrite growth, "dead" Li accumulation and undesirable solid electrolyte interphase during continuous Li plating/stripping [11], resulting in perishing cycling stability and potential safety hazards [12-15]. A crucial matter is the irregular electrochemical plating manner of Li metal during lithiation, and the spontaneous as-formed fragile solid electrolyte interphase (SEI) was broken and rebuilt on the account of its low interfacial energy, resulting in self-accelerated growth of Li dendrite, high interface resistance and low Coulombic efficiency (CE). Furthermore, the inherent deposition ablation feature of Li metal presents another major challenge to the infinite volumetric expansion effect of Li metal. A stable nucleation interface can not only alleviate the interface contact problem caused by deposition ablation of Li metal, but also effectively induce lithium metal plane deposition.

To settle the aforementioned problems, various strategies have been developed, and the focus has been predominantly on the interface engineering between the electrolyte and the electrode. A string of electrode/electrolyte interface engineering methods and artificial isolating layers have been proposed to induce the homogeneous Li plating and built robust SEI with high interfacial energy [16-22]. Building a conductive layer with lithiophilic sites has aroused great interests and is considered to be an effective way to overcome the technical matters

* Corresponding author.
E-mail address: xuxu@whut.edu.cn (X. Xu).
[1] X. C. and Z. L. contributed equally to this work.

https://doi.org/10.1016/j.cej.2022.136256
Received 25 January 2022; Received in revised form 14 March 2022; Accepted 5 April 2022
Available online 7 April 2022
1385-8947/© 2022 Elsevier B.V. All rights reserved.

associated with the formation of Li dendrite and notorious interphase side reaction [23-29]. A variety of lithiophilic materials have been demonstrated to homogenize Li deposition, such as metallic oxides (ZnO, CuO) [30,31], metal nanoparticles (Ag, Au, Zn) [32-35], nitrogen-doped carbons [36], and so on, which can lower the barrier of nucleation and confine nucleation-growth of metallic Li. However, the preferential deposition of Li metal at the top of the electrode associated with electronic and ionic transport remains a crucial issue [37-39], resulting in the great decrease of active site utilization and the deposition capacity. Recently, a three-dimensional (3D) lithiophilic-lithiophobic-lithiophilic dual-gradient porous skeleton was made public to achieve better regulation of metallic Li deposition and inhibit the development of dendrite [40]. Peng et al. reported a bottom-top channeling Li nucleation and growth by gradient lithiophilic 3D conductive host for Li metal anode [41]. Besides, a lithiophilic gradient ZnO/graphene/carbon nanotube (CNT) (G-ZGC) host has been reported to fulfil the outstanding chemical property of Li metal electrodes [42]. These commendable reports point out that the gradient design can skillfully solve the aforementioned problems and maximize the Li deposition capacity while achieving almost 100% utilization of different functional parts. Nevertheless, the existing gradient designs are commonly based on heavy metal porous frameworks, and complex preparation processes are usually required, seriously hindering the promotion of the volumetric and gravimetric energy densities and the practical application of LMBs. Notably, the development of the gradient structure within an individual nanostructure is highly desired for the practical applications of Li storage, which is applicable to the existing electrode processing method.

Carbon based materials are widely utilized in energy storage and conversion fields, owing to their mature production process and excellent stable physical and chemical properties. Hollow carbon nanostructures with interconnected porous channels derived from MOFs can be harvested by a simple, universal and high-yield synthesis method [43]. Attracted by the MOFs-derived carbon materials, the carbon nanotube interwoven polyhedrons (CNIP) with inside-out lithiophilic gradients are elaborately designed as stable Li metal host by annealing of ZIF-8@ZIF-67 core–shell precursors. Firstly, the derived CNT possesses good electronic conductivity and unclosed hollow structure for electrolyte penetration, providing bicontinuous pathways for electrons and Li ions. And the porous nanostructure provides enough space for Li metal deposition inside and reliefs the serious volume change in the repeated process of Li plating/stripping. Secondly, benefitting from the existence of the inside lithiophilic ZnO, the overpotential of Li nucleation is effectively decreased and Li metal will preferentially nucleate inside the polyhedron and deposit from inside to outside, which maximizes the space utilization of CNIP and eliminates the dendrite growth. Lastly, an optimized SEI is electrochemical formed because of unique nanostructure, which favors the fast transport Li ions and the inhibition of the lithium dendrite growth. The average CE is up to 98.2% (200 cycles) under 1 mA cm^{-2} in CNIP||Li half-cells, and long-term cycling for 1500 h in symmetrical cells under 3 mA cm^{-2} can be implemented. Remarkably, the CNIP-based Li metal anode is beneficial to long lifespan more than 300 cycles with 80% capacity retention at 1 C with nearly 100% CE, when paired with $LiFePO_4$ cathode with the areal mass loading of 18.3 mg cm^{-2}.

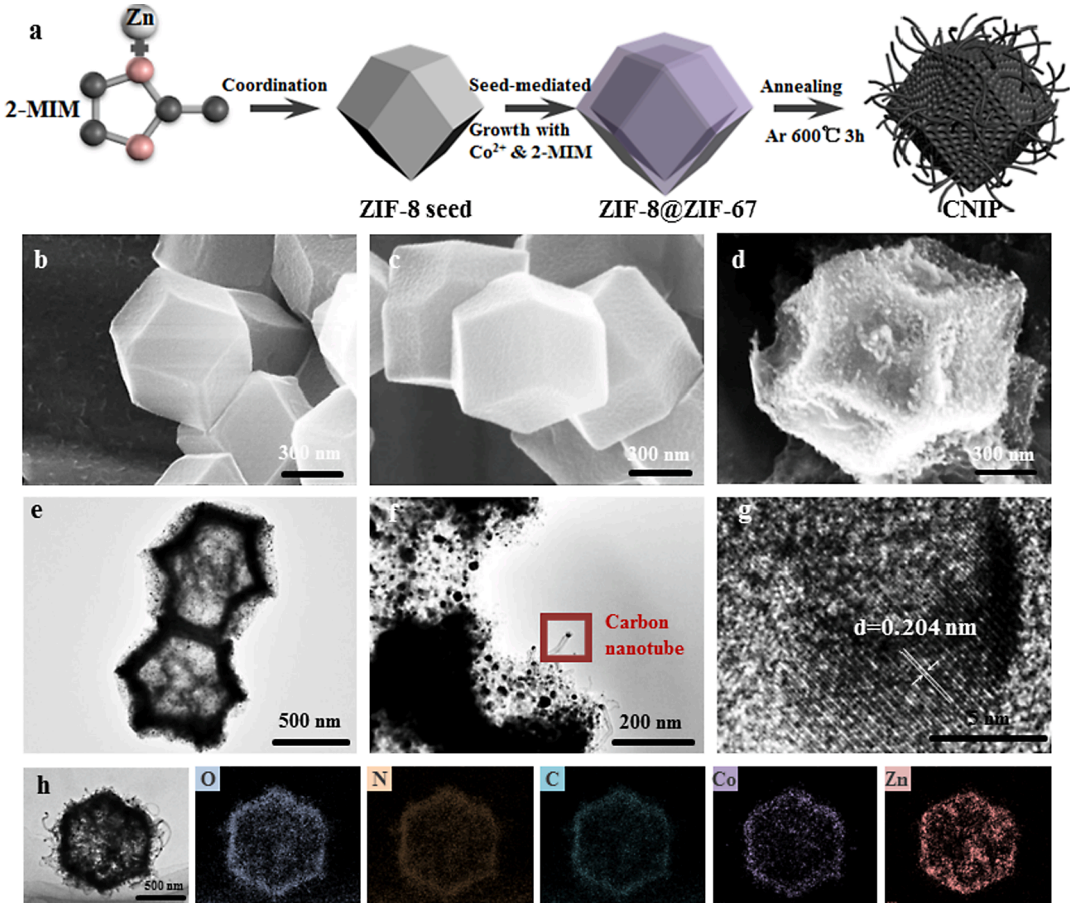

Fig. 1. (a) Mechanism schematic of the CNIP nanocomposite synthesis process. SEM images of (b) ZIF-8, (c) ZIF-8@ZIF-67 and (d) CNIP. (e-f) TEM images of CNIP. (g) HRTEM image of CNIP. (h) Elemental mappings of CNIP.

2. Results and discussion

2.1. Feature of CNIP polyhedrons

The schematic of the synthetic route for CNIP is shown in Fig. 1a. Firstly, uniform polyhedron ZIF-8 particles with the approximate size of 550 nm were synthesized by a typical solution method (Fig. 1b) [44]. ZIF-67 and ZIF-8 possess the identical topological structure, enabling the synthesis of ZIF-8@ZIF-67 core–shell nanoparticles with the average size of 580 nm (Fig. 1c). Fig. S1 clearly exhibits the powder XRD diffraction patterns of ZIF-8@ZIF-67, which well proves that the shell of ZIF-67 is successfully and uniformly coated on the surface of ZIF-8 crystal. The carbonization product is still homogeneous and its morphology basically maintains similar as the original crystals with an average size of about 900 nm (Fig. 1d). Whereas, the surface changes into rough and concave, which can be interpreted as the effect of the gas generated by the decomposition of ZIF-8@ZIF-67 precursors, propelling metal ions to outward and resulting in the formation of a hollow structure of porous shell (Fig. 1e) [43]. Interestingly, from the transmission electron microscopic (TEM) images (Fig. 1f and Fig. S2), these bumps composed of intimately and densely CNTs with a diameter of around 10 nm, which interwoven together to form the polyhedral carbon skeleton. The metallic cobalt (Co) nanoparticles uniformly anchor on the surface of ZIF8, which not only greatly contribute to the preservation of the shape of the polyhedron, but also catalyze the production of CNT from ethene with the existence of inert gas [45]. The lattice fringes with a d-spacing of 2.04 Å can be clearly observed by the measurement of high-resolution TEM (HRTEM) (Fig. 1g), matching with the (1 1 1) plane of metallic Co. As shown in Fig. 1h, the even distributions of the elements throughout CNIP indicate the homogeneity in the carbonization process. The distribution of Co element is concentrated in the outer shell, while Zn element can be still observed inside the nanostructure. The distribution tendencies of Zn and Co elements can be further verified in Fig. S3. In addition, Fig. S4 clearly verifies that Co

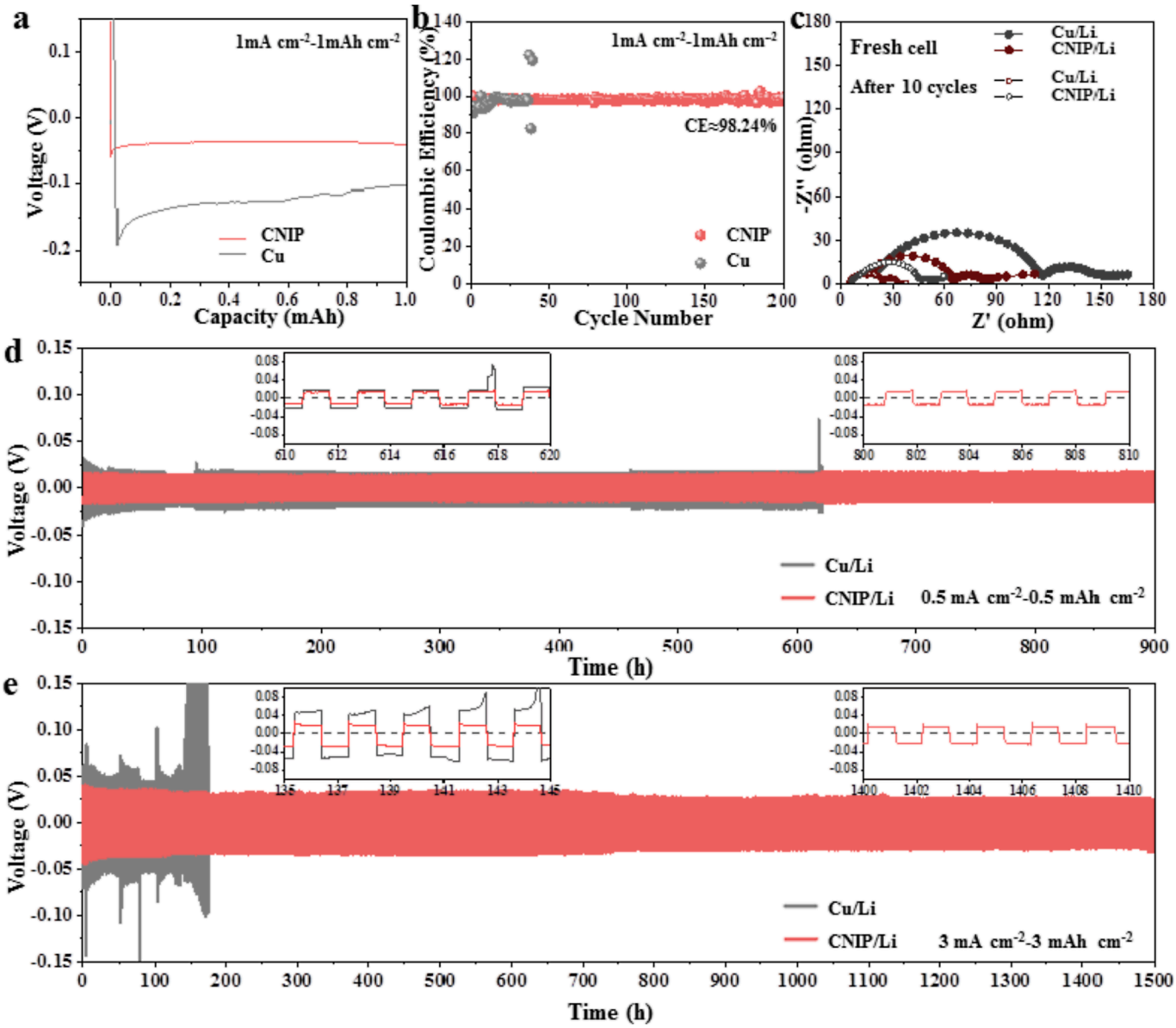

Fig. 2. (a) Nucleation overpotential of metallic Li for the pristine Cu and CNIP electrodes under 1 mAh cm^{-2}. (b) The comparison of CE between pristine Cu and CNIP electrodes at 1 mA cm^{-2} for 1 mAh cm^{-2}. (c) EIS of symmetrical cells. Hysteresis voltage images of symmetrical cells assembled with CNIP/Li electrodes and Cu/Li electrodes, measured under conditions of (d) 0.5 mA cm^{-2}-0.5 mAh cm^{-2} and (e) 3 mA cm^{-2}-3 mAh cm^{-2}. The magnified illustration exhibits voltage curves of certain cycles.

nanoparticles locate at the top of the outer carbon nanotubes. The decomposed products were measured by XRD (Fig. S5) to further study the phase structure of CNIP. A broad and weak diffraction peak at around 26° is consistent with the peak (0 0 2) of graphitic carbon [46]. No diffraction patterns related to Zn or Co compounds are detected, while the surface chemical states of CNIP can be explored through the analysis of X-ray photoelectron spectroscopy (XPS) (Fig. S6). The spectrum of Zn displays two peaks at 1044.3 eV and 1021.4 eV, which agrees well with the XPS spectra of Zn^{2+} of ZnO [47]. The N 1 s spectrum illustrates the graphitic-N in CNIP, which is able to promote the electron transfer. The surface area of the CNIP was measured by conducting the N_2 adsorption–desorption isotherms (Fig. S7), which is determined to be 148.6 m^2 g^{-1}. The high specific surface area is favorable to lower the local current density to homogenize Li deposition and reduce the effect of the volume change caused by the plating/stripping of Li metal in the process of charge/discharge.

2.2. Electrochemical performance of the standard half-cells

The initial nucleation process of metallic Li is of great importance for the following operation. The electrochemical performances of Cu||Li and CNIP||Li half-cells in ether electrolyte were firstly investigated. Fig. 2a illustrates the voltage-capacity curves for the initial deposition of metallic Li with CNIP and pristine Cu electrodes. In the initial stage of nucleation process, voltage precipitously dips to the lowest position and subsequently tends to plateaus for both electrodes. The nucleation overpotential, as prescribed as the gap falling in the lowest voltage and the plateau [48], was measured as 20 mV for CNIP electrode under a current density of 1 mA cm^{-2}, which is much smaller than that of pristine Cu (65 mV), evidencing the advantage of CNIP as Li nucleation facilitator and in favor of realizing high-efficiency Li plating/stripping behavior in the subsequent cycles. The declined nucleation overpotential should be contributed to the high specific surface area of porous framework, which alleviates local current density during Li deposition, in addition, the synergistic effect of ZnO, Co nanoparticles and lithiophilic heteroatom dopants effectively reduces the nucleation barrier. To study the plating/stripping behavior of metallic Li clearly, CE tests have been implemented. As shown in Fig. S8, the CNIP electrode exhibits a high and stable average CE of 98.4% over 350 cycles under a current density of 0.5 mA cm^{-2} for a capacity of 0.5 mAh cm^{-2}, superior to the pristine Cu foil for an average CE of 83.1% as well as a short cycle life of 120 cycles. Under the current density of 1 mA cm^{-2} for the capacity of 1 mAh cm^{-2}, CNIP hosted Li remains steady and high CE value of 98.24% for 200 cycles, exceeding pristine Cu electrode with an average CE of 70%, less than 40 cycles (Fig. 2b). Even at the 151st cycle, the CNIP electrode still retains a stable voltage polarization of 41 mV (Fig. S9), exhibiting the impressive reversibility of Li plating/stripping process. It is worth mentioning that, the initial CE is critical to the capacity retention rate of the battery. Moreover, overall capacity loss decides the cycle life and the actual energy density of the full battery. Fig. S10 shows the comparison of initial CE of the two electrodes under current densities of 0.5, 1, and 2 mA cm^{-2} with a plating/stripping capacity of 0.5, 1 and 2 mAh cm^{-2}, respectively. CNIP electrodes exhibit high average CE for 97.03%, 99.24% and 99.35% during the initial ten cycles. Table S1 intuitively reveals the vital influence of initial CE on capacity retention.

To investigate the concrete electrochemical mechanism and process of kinetic reaction of CNIP/Li, the electrodes of pristine Cu foil and CNIP were respectively plating with 5 mAh cm^{-2} of metallic Li under a current density of 0.5 mA cm^{-2} in advance. Then electrochemical impedance spectroscopy (EIS) was performed on symmetrical cells assembled with Cu/Li||Cu/Li and CNIP/Li||CNIP/Li respectively. As shown in Fig. 2c, the impedance spectra are combined of an intercept on the Z_0 axis at the high frequency region, representing the impedance of the electrolyte (R_s) connected with the assembly process of battery. The subsequent two flat semicircles are present in each curve, representing the SEI impedance (R_{SEI}) in the high-frequency region and the interfacial impedance of the electrode–electrolyte (R_{ct}) in the low-frequency region [49,50]. According to the equivalent circuit of cells (Fig. S11), impedance parameters (Table S2) are simulated, which exhibit the comparison between the fresh cells and the cells cycled for ten times. For R_{SEI}, the symmetrical cell with CNIP/Li electrodes manifests the lower value, no matter the fresh cell (43.4 Ω) or after 10 cycles symmetrical cell (20.2 Ω) and the latter exhibits the lowest value confirmed the presence of a stable and ion-diffusion favorable SEI layer. On the contrary, the higher R_{SEI} of Cu/Li symmetrical cell (53.7 Ω) and significant change after the operation of Cu/Li symmetrical cells (103.4 Ω) implying the repeated crack and reconstructed of SEI layer in the process of the charge/discharge cycles, which restrained the migration of Li^+ and ultimately resulted in the worse electrochemical performance. The R_{ct} of the fresh symmetrical cell with CNIP/Li electrodes is 5.4 Ω, which shows lower than that of the Cu/Li fresh symmetrical cell (20.5 Ω). Compared with the R_{ct} of the symmetrical cells with Cu/Li electrodes (27.5 Ω) after 10 cycles, the R_{ct} of the symmetrical cells with CNIP/Li electrodes is further decreased to 8.4 Ω, suggesting batter reaction kinetics at the contact interface between the electrode and electrolyte ascribed to the activation in the initial cycles.

In order to further verify the cycling stability of CNIP host, Fig. 2d shows the Galvanostatic voltage curves of the symmetrical batteries under a current density of 0.5 mA cm^{-2} for 0.5 mAh cm^{-2}. It is apparent that symmetrical batteries with CNIP/Li electrodes operated steady voltage hysteresis for over 900 h, displaying the good long-term cycling performance of CNIP host. Symmetrical cells with Cu/Li electrodes last for 630 h before the sharp fluctuation of voltage, and the failure is attributed to the formation of Li dendrite and repeated broken of SEI layer. As exhibited in the local magnified views at 520–570 h and 900–950 h, the symmetrical cell with CNIP/Li electrode shows a low polarization voltage of 11 mV, far less than that of the symmetrical cells with Cu/Li electrodes (25 mV). The symmetrical cells with Cu/Li electrodes show noisy voltage profiles with large over potentials at 150 h as the current density enhanced to 3 mA cm^{-2} for 3 mAh cm^{-2}. That is because the uncontrollable growth of Li dendrite significantly shortens the cycling span life of cells. In contrast, symmetrical cell with CNIP/Li electrodes exhibits a low polarization voltage of 22 mV and stable running for near 1500 h pleasantly (Fig. 2e), demonstrating the homogeneous deposition of metallic Li and efficient inhibition of dendritic Li.

2.3. Lithium deposition morphologies and structural stability

The morphology evolution and the volume expansion of the CNIP and pristine Cu electrodes after plating/stripping process were explored by characterization of ex situ SEM. Fig. 3a and b present the surface image of CNIP and pristine Cu electrodes harvested after discharging to 0.5 mAh cm^{-2}, respectively. CNIP nanoparticles are clearly observed, and no dendrite-like layers appeared even at the interface between copper foil and CNIP layer (Fig. S12), verifying that CNIP possesses a strong affinity toward Li and allows for the optimized Li deposition. In contrast, filament-shaped Li dendrites are observed at the surface of the pristine Cu electrode under the same condition, attributed to the heterogeneous deposition of metallic Li. Fig. 3c-d present the surface SEM images of the CNIP and pristine Cu electrodes obtained after 10 cycles of Li plating/stripping at 0.5 mA cm^{-2}-0.5 mAh cm^{-2} to verify the structural stability of electrodes. CNIP electrode still maintains a uniform and smooth surface (Fig. 3c), yet the columnar-shaped Li dendrites leading to the rough surface of the pristine Cu is observed (Fig. 3d), owing to selective deposition of Li [51,52]. The above phenomena prove that CNIP host stabilizes the structure of electrodes and suppresses the development of Li dendrite. The volume change of electrodes in the process of Li plating/stripping is worthy of further discussion. The thickness of the initial CNIP layer is 8 μm (Fig. S13), and it slightly increases to 11.1 μm after the deposition of Li metal with the capacity of 0.5 mAh cm^{-2} (Fig. 3e). Remarkably, even after ten cycles, the thickness

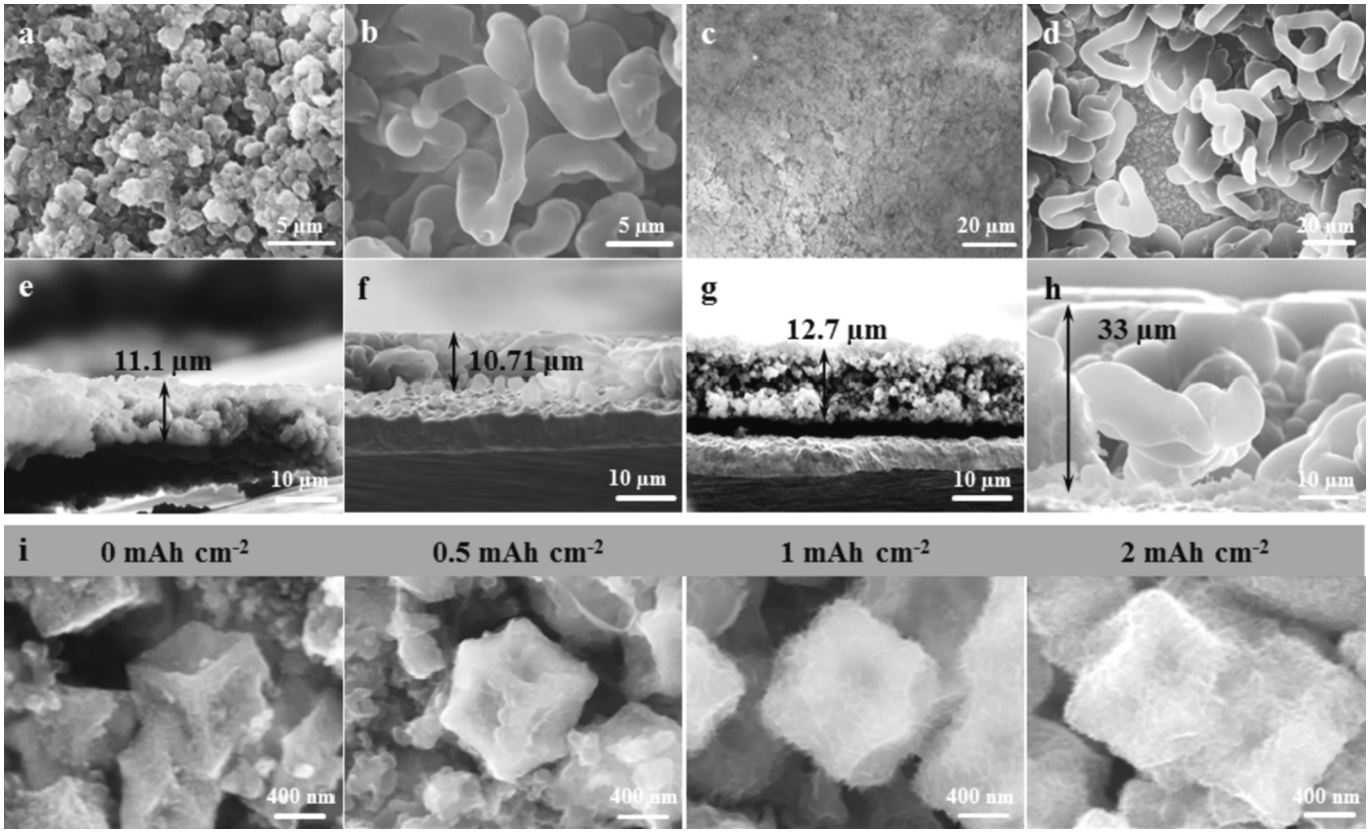

Fig. 3. Top views and cross-sectional views of (a, e) CNIP electrodes, (b, f) Cu electrodes plated with metallic Li for 0.5 mAh cm^{-2}, and (c, g) CNIP electrodes, (d, h) Cu electrodes plated/stripped with metallic Li after 10 cycles under 0.5 mA cm^{-2} for 0.5 mAh cm^{-2}. (i) SEM images of CNIP host after plating with different capacities of metallic Li.

only increases to 12.7 μm, suggesting the deposited Li remains intact and compact (Fig. 3g). Although there is no host on the pristine Cu to occupy any space, the thickness of dendrite Li grows to 10.71 μm after discharging to 0.5 mAh cm^{-2} (Fig. 3f), and it further dramatically increases to 33 μm after 10 cycles (Fig. 3h). We notice that the vast inactive lithium that remains on the copper foil after cycling is "dead Li", which is the culprit of the low CE [52]. By comparing the volume changes, it demonstrates that the CNIP layer affords a great inhibitory effect on the volume expansion of electrodes. Fig. 3i shows the morphological evolution of CNIP electrode to further explore the Li deposition behavior by plating different capacity of Li metal at a certain current density of 0.5 mA cm^{-2}. No significant changes are observed on the surface of the polyhedron particles after 1 h, which confirms the deposition of Li metal inside the polyhedrons (Fig. S14). After 2 h, the edges of the particles become vague and the particle size slightly increases, indicating that the metallic Li expands from inside to outside and begins to deposit on the outer surface of the polyhedron. After 4 h, the particles grow even larger and some of the gaps between the particles are also filled with the metallic Li, but the lithium dendrites never appear. The inside-outside plating process is attributed to the inside-out lithiophilic gradients and uniform nanostructure, although the volume of polyhedron is limited.

2.4. Electrode/electrolyte interface analysis

XPS analyses were performed on cycled electrodes and etched surface via Ar ion milling for 200 s to study the chemical composition of SEI. The CNIP and pristine Cu electrodes were disassembled from the half-cells after discharging for 0.5 mAh cm^{-2}. As displayed in Fig. 4, for the C 1 s spectra, both electrodes illustrate the commonly observed bonds, including C–C (~284.8 eV), C-O (~285.7 eV), C = O (~289.0 eV), COOR (~290.3 eV) as well as CF_X (~293 eV).[21] The existence of CF_3 (~688.5 eV) and CF (~687.3 eV) is identified more clearly in the F 1 s spectrum, and the other peak at ~ 684.9 eV corresponds to LiF, most likely resulting from LiTFSI [53-55]. For the Li 1 s spectra, peaks in the range of ~ 55–56 eV are assigned to LiF and Li_3N, while the Li_2O is observed. Besides, the spectra of O 1 s also exhibit little Li_2O content (Fig. S15). This can be attributed to the oxidation of Li metal on the electrode surface by air during sample preparation. Li-N species can be further confirmed in the spectrum of N 1 s with four tangled contributions (~407.4, ~404.0, ~399.7 and ~ 397.9 eV) correspond to $LiNO_2$, $Li_2N_2O_2$, Li_3N and LiN_xO_y, respectively [56,57]. In the Co 2p spectra, the original Co-N_x peaks (~780 and ~ 796 eV) emerge after sputtering for 50 s, which comes down to the separation of Co nanoparticles from the outside by the outer organic layer of SEI film after the discharge process [15]. After the top SEI layer was etched out, a peak at 282.5 eV in C 1 s spectrum for the both electrodes were explored and can be attributed to lithium carbides, which was supported by the reduction of Li metal to solvent, at the same time, the high amount of LiF is detected in those two electrodes. All that matter is, for the CNIP electrode, the LiF and Li_3N signals remain evident on the SEI-CNIP interface and persist throughout the whole etching process. This phenomenon shows the resulting inorganic layer of SEI is extremely uniform, which can be attributed to the unclosed hollow nanostructure and the contribution of lithiophilic gradient design in homogenizing lithium deposition. In addition, the peak intensity of Co-Li signal (59.6 eV) strengthens rapidly with increasing etching depth, along with heightening Co-N_x and Co signals in Co 2p spectrums, illustrating the formation of desirable SEI with uniform LiF/Li_3N-organic structure and the penetrating deposition of lithium. It is well known that LiF is one of the desirable components of SEI, which can be conductive to obtaining a F-rich SEI layer with high mechanical barrier against the growth of Li dendritic benefitted from its ultra-high mechanical strength (a shear modulus of 54.2 GPa) [58], In

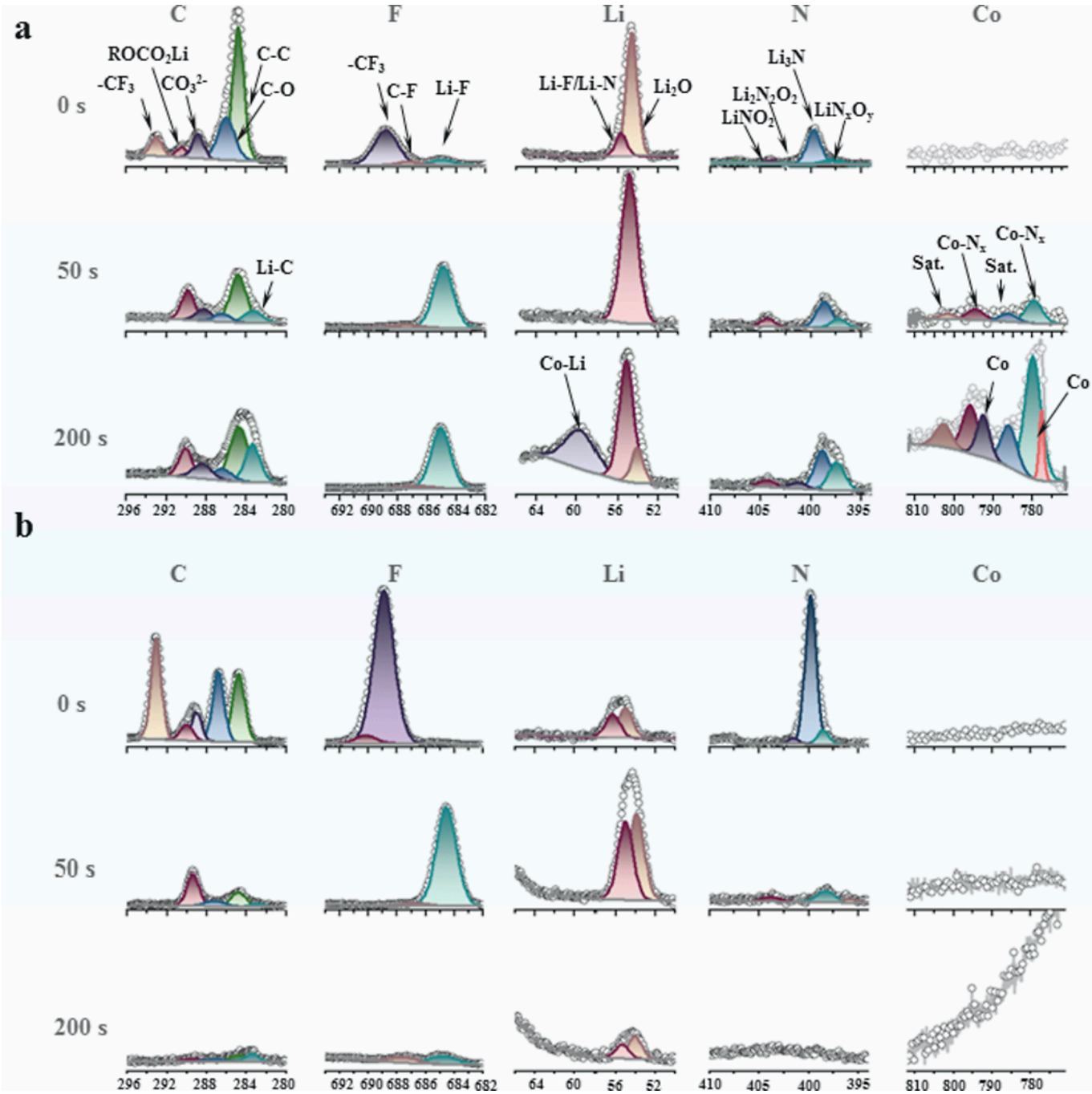

Fig. 4. Chemical components of SEI layer. XPS profiles of the cycled (a) CNIP and (b) Cu substrates after being etched for different times.

addition, the Li_3N, as known to process the highest Li^+ ionic conductivity among the common SEI components (~2×10^{-4} to 4×10^{-4} S cm^{-1}) [59], greatly favors the reduction of the resistance of the SEI layer. The above effects support the highly reversible stripping/plating of metallic Li even for long lifespan for the CNIP electrode. In contrast, for pristine Cu electrode, the C 1 s signal attenuates to the noise level before etching reaches the SEI-Cu interface, accompanied with a sharp decrease of the LiF signal and the disappearance of the Li_3N signal, predicting a non-uniform Li deposition process.

2.5. Electrochemical performance of full cells

To further explore the potential of practical applications for the CNIP electrode, full cells were assembled with CNIP/Li as the anode and $LiFePO_4$ (LFP) as the cathode. When the LFP loading is ~ 1.8 mg cm^{-2}, Fig. 5a displays the rate performance of full cells comprising the CNIP/Li and Cu/Li anodes, delivering similar discharge capacities at low current rates. While at high current rate of 5 C, the CNIP/Li||LFP full cell exhibits a capacity of 100 mAh g^{-1}, higher than Cu/Li anode (80 mAh g^{-1}). At 1 C, it is obvious that the cell with CNIP/Li electrode enables a superior capacity retention of 90.3% after 300 cycles (Fig. 5b). On the contrary, the capacities based on Cu/Li electrode decay rapidly after 160 cycles and 50 mAh g^{-1} is maintained after 300 cycles. Remarkably, even at a much higher LFP loading of 18.3 mg cm^{-2}, the outstanding rate capability and cycling stability of the CNIP/Li||LFP full cells are still delivered. As shown in Fig. 5c, at rates of 0.2 C, 1 C, and 5 C, the capacities of CNIP/Li||LFP cell are 153 (~2.8 mAh cm^{-2}), 133, and 83 mAh g^{-1}, respectively. The capacities are 107, 86, and 0 mAh g^{-1} for the

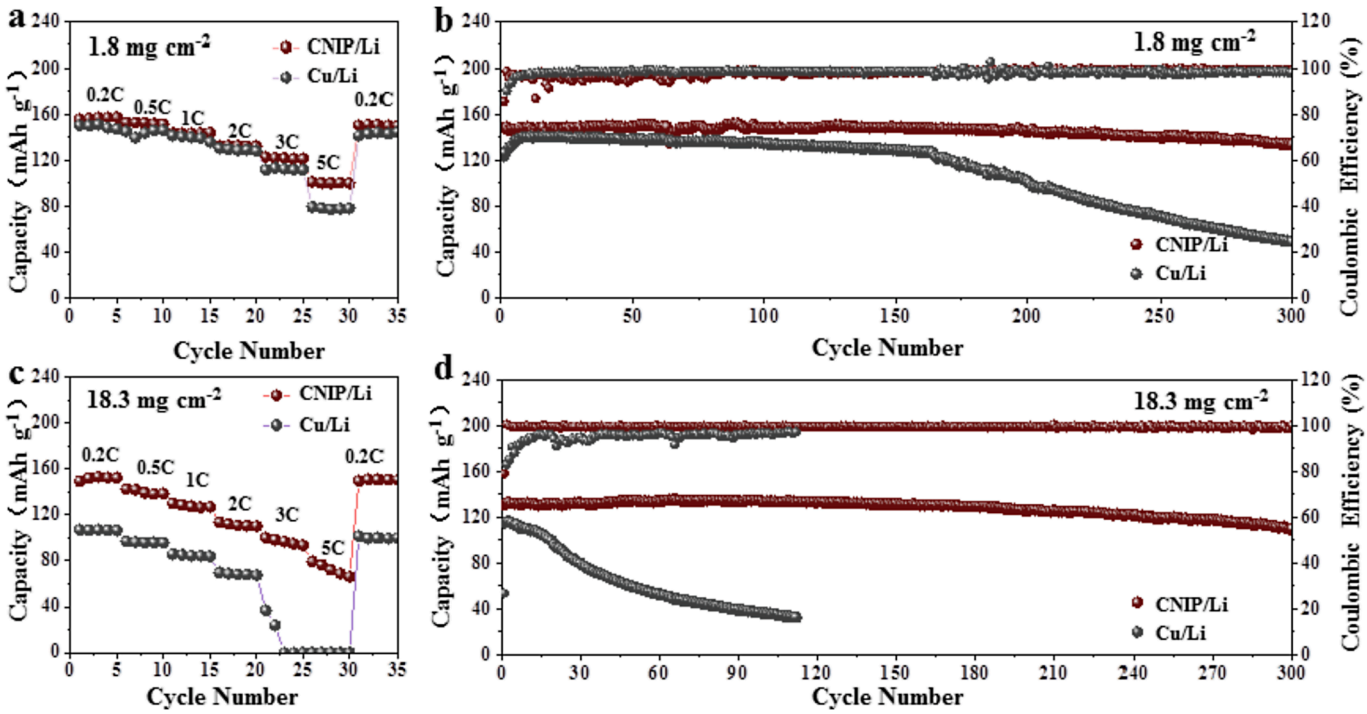

Fig. 5. Electrochemical performance of full batteries paired with the LFP cathode. (a) Rate performance and (b) cycling performance at 1 C of full cells with LFP with the mass loading of 1.8 mg cm^{-2}. (c) Rate performance and (d) cycling performance at 1 C of full cells with LFP with the mass loading of 18.3 mg cm^{-2}.

cell containing Cu/Li anode under the same test conditions. Long-term cycling performance was further conducted at 1 C, and the results indicate that CNIP/Li||LFP full cells enable high capacity in initial cycles (133 mAh g^{-1}) and the capacity keeps steady in the following test process. The capacity retention of 82.7% is obtained after 300 cycles. Nevertheless, Cu/Li||LFP cells can merely show a capacity of 116 mAh g^{-1} at the initial cycle, which rapidly fades to 60 mAh g^{-1} after 50 cycles (Fig. 5d). Additionally, the CNIP/Li||LFP full cells present a lower voltage hysteresis at different current rates (Fig. S16). Ascribed to the uniform deposition of metallic Li and small volume change during cycling, CNIP electrode is proved feasible for practical applications.

3. Conclusion

In summary, carbon nanotube interwoven polyhedrons (CNIP) were synthesized as lithium metal host via annealing ZIF-8@ZIF-67 core–shell structure. The lithiophilic ZnO derived from ZIF-8 mainly localizes in the inner part, while the outer layer of the carbon polyhedron is rich in Co-catalyzed carbon nanotube, which forms an inside-out lithiophilic gradient, inducing the preferential deposition of metallic Li inside the polyhedron. Combining with the low local current density provided by the conducting and unclosed carbon nanotube network, this unique nanostructure efficiently inhibits the growth of Li dendrite and maximizes the space utilization of the polyhedron. Moreover, an optimized SEI formed on the cycled CNIP is proved by XPS with different etching times, which benefits for the fast transport Li ions and the inhibition of the lithium dendrite growth. Remarkably, when paired with LFP cathode with high mass loading of 18.3 mg cm^{-2}, the CNIP-based Li metal anode can cycle for 300 cycles with 80% capacity retention at 1 C, with nearly 100% CE.

Declaration of Competing Interest

The authors declare that they have no known competing financial interests or personal relationships that could have appeared to influence the work reported in this paper.

Acknowledgements

This work was supported by the National Natural Science Foundation of China (51702247), the Fundamental Research Funds for the Central Universities (WUT: 2021IVA123, 2021III009JC, 2021III013GL), the Hainan Provincial Joint Project of Sanya Yazhou Bay Science and Technology City (520LH056), Sanya Science and Education Innovation Park of Wuhan University of Technology (2020KF0021), and State Key Laboratory of Advanced Technology for Materials Synthesis and Processing (WUT:2021-ZD-1).

Appendix A. Supplementary data

Supplementary data to this article can be found online at https://doi.org/10.1016/j.cej.2022.136256.

References

[1] V. Etacheri, R. Marom, R. Elazari, G. Salitra, D. Aurbach, Energy Environ. Sci. 4 (2011) 3243–3262.
[2] S. Stauss, I. Honma, Bull. Chem. Soc. Jpn. 91 (2018) 492–505.
[3] A. Noori, M.F. El-Kady, M.S. Rahmanifar, R.B. Kaner, M.F. Mousavi, Chem. Soc. Rev. 48 (2019) 1272–1341.
[4] Z. Wei, Y. Ren, J. Sokolowski, X. Zhu, G. Wu, InfoMat 2 (2020) 483–508.
[5] M. Watanabe, K. Dokko, K. Ueno, M.L. Thomas, Bull. Chem. Soc. Jpn. 91 (2018) 1660–1682.
[6] J.W. Choi, D. Aurbach, Nat. Rev. Mater. 1 (2016) 16013.
[7] C. Fang, X. Wang, Y.S. Meng, Trends Chem. 1 (2019) 152–158.
[8] A. Rosenman, E. Markevich, G. Salitra, D. Aurbach, A. Garsuch, F.F. Chesneau, Adv. Energy Mater. 5 (2015) 1500212.
[9] A. Hu, M. Zhou, T. Lei, Y. Hu, X. Du, C. Gong, C. Shu, J. Long, J. Zhu, W. Chen, X. Wang, J. Xiong, Adv. Energy Mater. 10 (2020) 2002180.
[10] P.G. Bruce, S.A. Freunberger, L.J. Hardwick, J.M. Tarascon, Nat. Mater. 11 (2011) 19–29.
[11] D. Lin, Y. Liu, Y. Cui, Nat. Nanotechnol. 12 (2017) 194–206.
[12] Y. Zhang, P. Zhang, S. Zhang, Z. Wang, N. Li, S.R.P. Silva, G. Shao, InfoMat 3 (2021) 790–813.
[13] S. Wu, K. Zhu, J. Tang, K. Liao, S. Bai, J. Yi, Y. Yamauchi, M. Ishida, H. Zhou, Energy Environ. Sci. 9 (2016) 3262–3271.
[14] J. Alvarado, M.A. Schroeder, T.P. Pollard, X. Wang, J.Z. Lee, M. Zhang, T. Wynn, M. Ding, O. Borodin, Y.S. Meng, K. Xu, Energy Environ. Sci. 12 (2019) 780–794.
[15] X.B. Cheng, R. Zhang, C.Z. Zhao, Q. Zhang, Chem. Rev. 117 (2017) 10403–10473.

[16] Y. Yao, X. Zhang, B. Li, C. Yan, P. Chen, J. Huang, Q. Zhang, InfoMat 2 (2019) 379–388.
[17] N.W. Li, Y.X. Yin, C.P. Yang, Y.G. Guo, Adv. Mater. 28 (2016) 1853–1858.
[18] F. Liu, Q. Xiao, H.B. Wu, L. Shen, D. Xu, M. Cai, Y. Lu, Adv. Energy Mater. 8 (2018) 1701744.
[19] H. Xia, Q. Xie, Y. Tian, Q. Chen, M. Wen, J. Zhang, Y. Wang, Y. Tang a, S. Zhang, Nano Energy 84 (2021) 105877.
[20] K. Tang, A. Du, S. Dong, Z. Cui, X. Liu, C. Lu, J. Zhao, X. Zhou, G. Cui, Adv. Mater. 32 (2020) 1904987.
[21] J. Zheng, M.H. Engelhard, D. Mei, S. Jiao, B.J. Polzin, J.-G. Zhang, W. Xu, Nat. Energy 2 (2017) 17012.
[22] T. Dong, J. Zhang, G. Xu, J. Chai, H. Du, L. Wang, H. Wen, X. Zang, A. Du, Q. Jia, X. Zhou, G. Cui, Energy Environ. Sci. 11 (2018) 1197–1203.
[23] A. Hu, W. Chen, X. Du, Y. Hu, T. Lei, H. Wang, L. Xue, Y. Li, H. Sun, Y. Yan, J. Long, C. Shu, J. Zhu, B. Li, X. Wang, J. Xiong, Energy Environ. Sci. 14 (2021) 4115–4124.
[24] L.L. Lu, J. Ge, J.N. Yang, S.M. Chen, H.B. Yao, F. Zhou, S.H. Yu, Nano Lett. 16 (2016) 4431–4437.
[25] Z. Qi, J. Tang, S. Misra, C. Fan, P. Lu, J. Jian, Z. He, V.G. Pol, X. Zhang, H. Wang, Nano Energy 69 (2020), 104381.
[26] T. Wang, R. Villegas Salvatierra, A.S. Jalilov, J. Tian, J.M. Tour, ACS Nano 11 (2017) 10761–10767.
[27] K. Yan, B. Sun, P. Munroe, G. Wang, Energy Storage Mater. 11 (2018) 127–133.
[28] Q. Yun, Y.B. He, W. Lv, Y. Zhao, B. Li, F. Kang, Q.H. Yang, Adv. Mater. 28 (2016) 6932–6939.
[29] G. Zheng, S.W. Lee, Z. Liang, H.W. Lee, K. Yan, H. Yao, H. Wang, W. Li, S. Chu, Y. Cui, Nat. Nanotechnol. 9 (2014) 618–623.
[30] C. Jin, O. Sheng, J. Luo, H. Yuan, C. Fang, W. Zhang, H. Huang, Y. Gan, Y. Xia, C. Liang, J. Zhang, X. Tao, Nano Energy 37 (2017) 177–186.
[31] K. Huang, Z. Li, Q. Xu, H. Liu, H. Li, Y. Wang, Adv. Energy Mater. 9 (2019) 1900853.
[32] P. Xue, S. Liu, X. Shi, C. Sun, C. Lai, Y. Zhou, D. Sui, Y. Chen, J. Liang, Adv. Mater. 30 (2018) 1804165.
[33] C. Yang, Y. Yao, S. He, H. Xie, E. Hitz, L. Hu, Adv. Mater. 29 (2017) 1702714.
[34] S. Wu, Z. Zhang, M. Lan, S. Yang, J. Cheng, J. Cai, J. Shen, Y. Zhu, K. Zhang, W. Zhang, Adv. Mater. 30 (2018) 1705830.
[35] F. Zhang, X. Liu, M. Yang, X. Cao, X. Huang, Y. Tian, F. Zhang, H. Li, Nano Energy 69 (2020), 104443.
[36] R. Zhang, X.R. Chen, X. Chen, X.B. Cheng, X.Q. Zhang, C. Yan, Q. Zhang, Angew. Chem. Int. Ed. 56 (2017) 7764–7768.
[37] D. Aurbach, E. Zinigrad, H. Teller, P. Dan, J. Electrochem. Soc. 147 (2000) 1274–1279.
[38] J. Zhang, H. Chen, M. Wen, K. Shen, Q. Chen, G. Hou, Y. Tang, Adv. Funct. Mater. 2110110 (2021).
[39] D. Zhang, A. Dai, B. Fan, Y. Li, K. Shen, T. Xiao, G. Hou, H. Cao, X. Tao, Y. Tang, ACS Appl. Mater. Interfaces 12 (2020) 31542-31551.
[40] H. Zheng, Q. Zhang, Q. Chen, W. Xu, Q. Xie, Y. Cai, Y. Ma, Z. Qiao, Q. Luo, J. Lin, L. Wang, B. Qu, B. Sa, D. Peng, J. Mater. Chem. A 8 (2020) 313–322.
[41] X. Yan, Q. Zhang, W. Xu, Q. Xie, P. Liu, Q. Chen, H. Zheng, L. Wang, Z. Zhu, D. Peng, J. Mater. Chem. A 8 (2020) 1678–1686.
[42] J. Zhou, F. Wu, G. Wei, Y. Hao, Y. Mei, L. Li, M. Xie, R. Chen, J. Power Sources 495 (2021), 229773.
[43] J. Meng, C. Niu, L. Xu, J. Li, X. Liu, X. Wang, Y. Wu, X. Xu, W. Chen, Q. Li, Z. Zhu, D. Zhao, L. Mai, J. Am. Chem. Soc. 139 (2017) 8212–8221.
[44] B.Y. Xia, Y. Yan, N. Li, H.B. Wu, X.W. Lou, X. Wang, Nat. Energy 1 (2016) 15006.
[45] J.P. Tessonnier, M. Becker, W. Xia, F. Girgsdies, R. Blume, L. Yao, D.S. Su, M. Muhler, R. Schlögl, ChemCatChem 2 (2010) 1559–1561.
[46] F. Liu, R. Xu, Z. Hu, S. Ye, S. Zeng, Y. Yao, S. Li, Y. Yu, Small 15 (2019) 1803734.
[47] A. Gu, J. Chen, Q. Gao, M.M. Khan, P. Wang, Y. Jiao, Z. Zhang, Y. Liu, Y. Yang, Appl. Surf. Sci. 516 (2020), 146160.
[48] Y. Lai, Y. Zhao, W. Cai, J. Song, Y. Jia, B. Ding, J. Yan, Small 15 (2019) 1905171.
[49] Z.Y. Wang, Z.X. Lu, W. Guo, Q. Luo, Y.H. Yin, X.B. Liu, Y.S. Li, B.Y. Xia, Z.P. Wu, Adv. Mater. 33 (2021) 2006702.
[50] L. Yue, S. Wang, X. Zhao, L. Zhang, J. Mater. Chem. 22 (2012) 1094–1099.
[51] K. Yan, Z. Lu, H.-W. Lee, F. Xiong, P.-C. Hsu, Y. Li, J. Zhao, S. Chu, Y. Cui, Nat. Energy 1 (2016) 16010.
[52] H. Yang, C. Guo, A. Naveed, J. Lei, J. Yang, Y. Nuli, J. Wang, Energy Storage Mater. 14 (2018) 199–221.
[53] S. Xiong, K. Xie, Y. Diao, X. Hong, J. Power Sources 246 (2014) 840–845.
[54] D. Aurbach, E. Pollak, R. Elazari, G. Salitra, C.S. Kelley, J. Affinito, J. Electrochem. Soc. 156 (2009) A694–A702.
[55] G. Wang, X. Xiong, D. Xie, X. Fu, X. Ma, Y. Li, Y. Liu, Z. Lin, C. Yang, M. Liu, Energy Storage Mater. 23 (2019) 701–706.
[56] D. Ensling, M. Stjerndahl, A. Nytén, T. Gustafsson, J.O. Thomas, J. Mater. Chem. 19 (2009) 82–88.
[57] A. Zhang, X. Fang, C. Shen, Y. Liu, C. Zhou, Nano Res. 9 (2016) 3428–3436.
[58] H. Shin, J. Park, S. Han, A.M. Sastry, W. Lu, J. Power Sources 277 (2015) 169–179.
[59] T. Lapp, S. Skaarup, A. Hooper, Solid State Ionics 11 (1983) 97–103.